Strain-tunable metamagnetic critical endpoint in Mott insulating rare-earth titanates

Zhentao Wang [1], Dominique Gautreau [1,2], Turan Birol [2] and Rafael M. Fernandes [1]
[1] *School of Physics and Astronomy, University of Minnesota, Minneapolis, Minnesota 55455, USA*
[2] *Chemical Engineering and Materials Science, University of Minnesota, Minneapolis, Minnesota 55455, USA*

(Received 4 May 2021; revised 24 January 2022; accepted 21 March 2022; published 5 April 2022)

Rare-earth titanates are Mott insulators whose magnetic ground state—antiferromagnetic (AFM) or ferromagnetic (FM)—can be tuned by the radius of the rare-earth element. Here, we combine phenomenology and first-principles calculations to shed light on the generic magnetic phase diagram of a chemically substituted titanate on the rare-earth site that interpolates between an AFM and a FM state. Octahedral rotations present in these perovskites cause the AFM order to acquire a small FM component—and vice-versa—removing any multicritical point from the phase diagram. However, for a wide parameter range, a first-order metamagnetic transition line terminating at a critical endpoint survives inside the magnetically ordered phase. Like the liquid-gas transition, a Widom line emerges from the endpoint, characterized by enhanced fluctuations. In contrast to metallic FMs, this metamagnetic transition involves two symmetry-equivalent and insulating canted spin states. Moreover, instead of a magnetic field, we show that uniaxial strain can be used to tune this transition to zero temperature, inducing a quantum critical endpoint.

DOI: 10.1103/PhysRevB.105.144404

Magnetic quantum phase transitions (QPTs) are often associated with exotic phenomena [1], from strange metallic behavior to possible deconfined quantum criticality [2–8]. Mott insulating perovskites, such as cuprates, iridates, ruthenates, and titanates, are promising candidates to study such QPTs since many of the pristine compounds display some type of antiferromagnetic (AFM) order [9,10]. To suppress the AFM transition temperature and attempt to induce a QPT, it is often necessary to dope the compounds, which also favors a metallic state over the Mott phase.

A remarkable exception are the rare-earth titanates $A\mathrm{TiO_3}$, where A denotes a rare-earth element [11]. By changing the ionic radius of A, the ground state interpolates between an AFM (of the G type, i.e., a Néel AFM) Mott insulating phase for larger radii (from Sm to La) and a ferromagnetic (FM) Mott insulating phase for smaller radii (from Yb to Gd) [12–18], see Fig. 1. While the magnetism arises from the Ti^{3+} $3d^1$ state, the size of A strongly affects the rotations of the $\mathrm{TiO_6}$ octahedra, which in turn impact the Ti orbital degrees of freedom [19]. The latter are believed to drive the change from AFM to FM, although the precise mechanism remains under debate [11,20–25].

This phenomenology suggests a potential path to realize magnetic QPTs while remaining inside the Mott insulating state via isovalent chemical substitution on the rare-earth site [26,27], such as in $\mathrm{Sm_{1-x}Gd_xTiO_3}$ [16] and $\mathrm{Y_{1-x}La_xTiO_3}$ [12,14,17,18]. In principle, there are several possibilities for magnetic QPTs: split transitions from either the AFM or the FM phase to the paramagnetic (PM) phase; split transitions from the AFM or FM phases to a coexistent AFM + FM state; a single first-order AFM-to-FM transition; or a single second-order AFM-to-FM transition, which would require fine tuning of parameters.

There is, however, one important ingredient that qualitatively changes this scenario: $A\mathrm{TiO_3}$, as several other perovskites, are not cubic materials but orthorhombic because of the pattern of the $\mathrm{TiO_6}$ octahedral rotations shown in Fig. 2(a). The corresponding *Pbnm* crystal structure generally promotes an admixture between the AFM and FM order parameters [28,29], indicating that most, if not all, $A\mathrm{TiO_3}$ pristine compounds display the same mixed AFM + FM phase—a canted spin state, as shown in Fig. 1. At first sight, this seems to challenge the notion that a QPT can be induced via substitution on the rare-earth site: since the phases of the end compounds are symmetry equivalent, the only difference is on the relative amplitudes between the AFM and FM order parameters (and therefore on the canting angle).

In this paper, we combine a phenomenological analysis with first-principles calculations to show that this is not the case and that a metamagnetic quantum critical endpoint (QCEP) could still be realized, particularly in the phase diagrams of $\mathrm{Sm_{1-x}Gd_xTiO_3}$ and $\mathrm{Y_{1-x}La_xTiO_3}$ [12–18]. The key point is that the staggered rotation between neighboring $\mathrm{TiO_6}$ octahedra, known as the R_5^- mode and illustrated in the right panel of Fig. 2(a), causes an admixture of the AFM and FM order parameters. Microscopically, this effect arises from the changes in the orbital level splittings promoted by the octahedral rotations, which in turn induce magnetic exchange anisotropies as well as the displacement of the oxygen ions from the middle of nearest neighbor titanium pairs, which induces antisymmetric exchange interactions. Because of this admixture, the would-be first-order transition line from the AFM to the FM state splits from the PM phase boundary, as shown schematically in Fig. 1. This first-order line, denoted by the dashed line in Fig. 1, ends in a critical endpoint (CEP, pink dot in Fig. 1), above which a Widom line emerges, analogous to the liquid-gas phase transition [30–32].

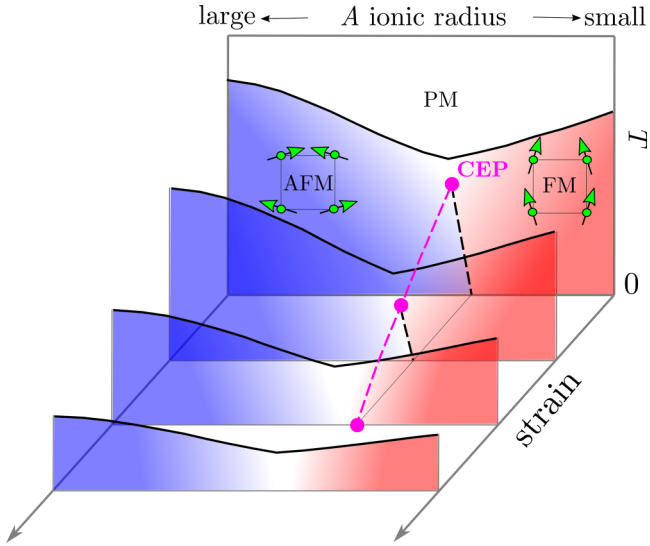

FIG. 1. Schematic magnetic phase diagram of Mott insulating rare-earth titanates $ATiO_3$ as a function of applied uniaxial strain. The horizontal axis refers to the average rare-earth radius in both stoichiometric and chemically substituted compounds such as $Sm_{1-x}Gd_xTiO_3$ and $Y_{1-x}La_xTiO_3$. At low temperatures, the transition between the antiferromagnetic (AFM)-dominated (blue shaded) and the ferromagnetic (FM)-dominated (red shaded) states is first order. Due to the TiO_6 octahedral rotations, however, the first-order line (black dashed line) terminates at a critical endpoint (CEP, magenta dot) before reaching the paramagnetic (PM) phase boundary. The CEP can in principle be tuned to $T = 0$ by external strain, resulting in a quantum critical endpoint (QCEP). The green arrows show schematically the canted spin configurations in the AFM- and FM-dominated states.

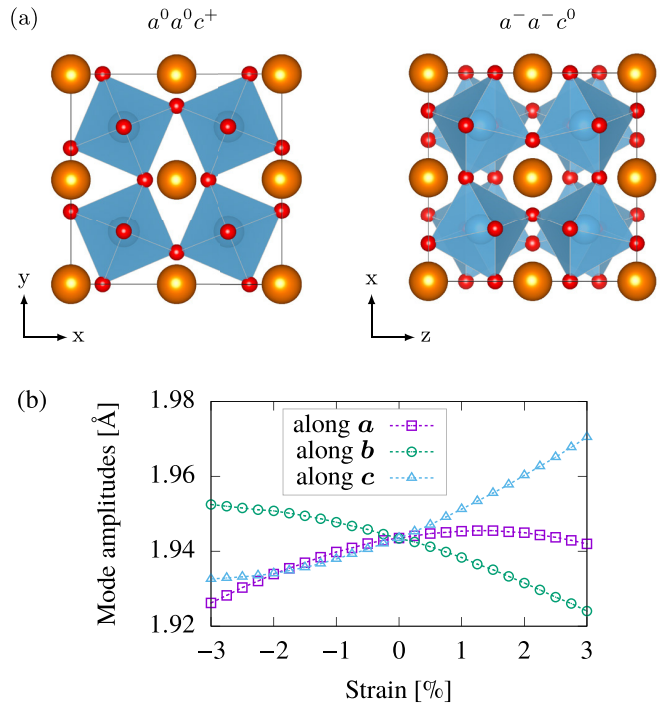

FIG. 2. (a) Schematics of the two types of octahedral rotation patterns in rare-earth titanates: in the Glazer notation, they are the $a^0a^0c^+$ pattern (left, which transforms like M_2^+), and the $a^-a^-c^0$ pattern (right, which transforms like R_5^-). Here, x, y, and z refer to the cubic axes. (b) Change in the amplitude of the R_5^- mode as a function of uniaxial strain along three different orthorhombic axes of $YTiO_3$.

The relevant order parameter associated with this transition is not the individual AFM or FM order parameters but the canting angle θ between the uniform and the staggered magnetizations. As illustrated in Fig. 1, θ changes from $\theta \gtrsim 0$ deep inside the AFM-dominated phase to $\theta \lesssim \pi/2$ inside the FM-dominated phase. While θ changes continuously when the phase diagram is traversed above the CEP (but below the magnetic ordering temperature), it undergoes a first-order jump below the CEP, signaling a metamagnetic transition. Such a metamagnetic transition, driven by octahedral rotations of a Mott insulator and characterized by a jump in the canting angle, is an unexplored counterpart of the widely studied magnetic-field-driven metamagnetic transition that occurs in metallic FMs, which is signaled by a jump in the uniform magnetization [33]. Remarkably, while the latter can be tuned to $T = 0$ by a magnetic field, we show that the CEP uncovered here can be tuned to a QCEP by uniaxial strain. This result is a direct consequence of the sensitivity of the octahedral rotation mode amplitude to strain, which we demonstrate using first-principles calculations [Fig. 2(b)]. Because strain has been routinely applied in strongly correlated systems via a variety of experimental setups [34–38]—including recently in rare-earth titanates [39]—our results provide a concrete recipe to promote a QCEP in Mott insulating, magnetically ordered perovskites.

We start by considering the artificial case where there is no spin-orbit coupling and the octahedral rotations can be neglected, implying a cubic crystal structure for $ATiO_3$ (space group $Pm\bar{3}m$). In this case, the FM and AFM order parameters transform as vectors under the O(3) spin-rotational group and are denoted respectively by $\boldsymbol{m}$ and $\boldsymbol{n}$. The only restriction we impose on the AFM wave vector $\boldsymbol{Q}$ is that $2\boldsymbol{Q} = 0$, which encompasses the configurations known as G type: $\boldsymbol{Q} = (\pi, \pi, \pi)$, C type: $\boldsymbol{Q} = (\pi, \pi, 0)$, and A type: $\boldsymbol{Q} = (0, 0, \pi)$. In terms of this artificial cubic lattice, they correspond to the momenta R, M, and X, respectively. The most general Ginzburg-Landau (GL) free energy expansion is given by

$$f = \frac{a_F}{2}m^2 + \frac{1}{4}m^4 + \frac{a_A}{2}n^2 + \frac{1}{4}n^4 + \frac{\gamma_1}{2}m^2n^2 + \frac{\gamma_2}{2}(\boldsymbol{m}\cdot\boldsymbol{n})^2. \tag{1}$$

Here, $a_F = a_{F,0}(T - T_F)$ and $a_A = a_{A,0}(T - T_A)$, where T_F and T_A are the bare FM and AFM ordering temperatures, respectively, and γ_i are Landau parameters. Note that we set the positive quartic coefficients of m^4 and n^4 to 1, which can always be done upon rescaling the other parameters. To traverse between the AFM and FM phases, we consider an abstract parameter ϵ, which is a function of the relative concentration of a substituted rare-earth element (as in the cases of $Sm_{1-x}Gd_xTiO_3$ and $Y_{1-x}La_xTiO_3$) and encompasses not only the structural but also the chemical effects of rare-earth substitution [40]. As a result, both T_F and T_A are implicit functions of ϵ. The available experimental phase diagrams

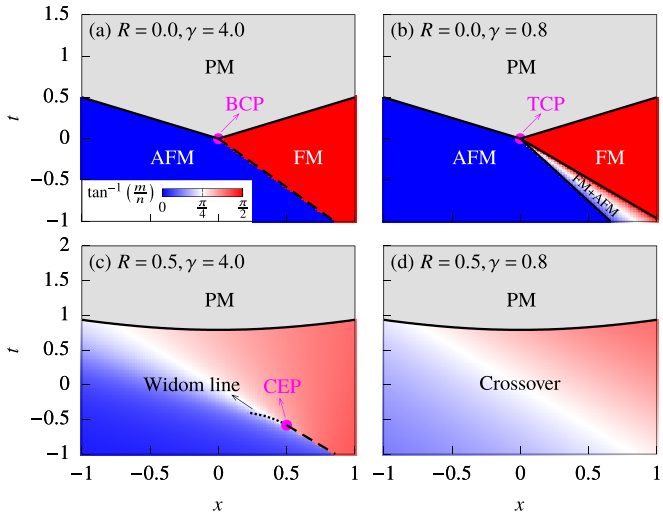

FIG. 3. Phase diagrams obtained by minimizing the free-energy Eq. (3) with $a = 0.4$. The solid (dashed) lines correspond to second (first)-order transitions. The dotted line in (c) is the Widom line, defined by the local maxima in the specific heat [see Fig. 4(d)].

of isolavent-substituted rare-earth titanates indicate that T_F and T_A cross with opposite slopes at ϵ^*, i.e., $T_F(\epsilon^*) = T_A(\epsilon^*)$. Near this multicritical point, it is convenient to parametrize the quadratic coefficients as

$$a_F = a\Big(t - \frac{x}{2}\Big), \qquad a_A = \Big(t + \frac{x}{2}\Big), \tag{2}$$

where we defined $t \equiv \tilde{T} - \frac{\tilde{T}_F + \tilde{T}_A}{2}$, $x \equiv \tilde{T}_F - \tilde{T}_A$, $a \equiv a_{F,0}/a_{A,0}$, and $\tilde{T} \equiv a_{A,0} T$. Note that x, not to be confused with doping, is implicitly related to the distance to the multicritical point as $x \approx (\frac{\partial \tilde{T}_F}{\partial \epsilon} - \frac{\partial \tilde{T}_A}{\partial \epsilon})(\epsilon - \epsilon^*)$.

A straightforward minimization of Eq. (1) shows that the nature of the multicritical point depends on the parameter $\gamma \equiv \gamma_1 + \min(\gamma_2, 0)$, being either a bicritical point (BCP) for $\gamma > 1$ or a tetracritical point (TCP) for $\gamma < 1$ [41,42]. In the former case, shown in Fig. 3(a), the AFM and FM phases are separated by a single first-order transition (dashed line). In the latter, displayed in Fig. 3(b), there is an intermediate AFM + FM coexistence phase, separated from the pure AFM and FM phases by two second-order transitions (solid lines).

We proceed by first turning on the spin-orbit coupling while keeping the octahedra unrotated. Now, $\boldsymbol{m}$ and $\boldsymbol{n}$ must transform according to the magnetic irreducible representations (irreps) associated with the cubic $Pm\bar{3}m$ space group. The FM and G-type AFM order parameters can still be parametrized by three-component vectors, as they transform according to the three-dimensional (3D) irreps $m\Gamma_4^+$ and mR_5^-, respectively. On the other hand, in the case of C- and A-type orders, the AFM order parameter splits in a one-dimensional (1D) little-group irrep (mM_2^+ and mX_1^-, respectively) plus a two-dimensional (2D) little-group irrep (mM_5^+ and mX_5^-, respectively) depending on whether the magnetization is parallel or perpendicular to the wave vectors M and X, respectively.

We are now in position to include the effects of the octahedral rotations that lower the space group from cubic to the orthorhombic $Pbnm$ (or equivalently $Pnma$ in the standard setting, see Appendix A for details). There are two types of octahedral rotations in the rare-earth titanates (as in most perovskites), which transform as the R_5^- and M_2^+ irreps of the cubic group $Pm\bar{3}m$ [Fig. 2(a)]. As shown in Appendix A, symmetry makes these modes necessarily couple bilinearly one component of the FM order parameter $\boldsymbol{m} = (m_a, m_b, m_c)$ to orthogonal components of two AFM order parameters $\boldsymbol{n}^{(\mu)} = (n_a^{(\mu)}, n_b^{(\mu)}, n_c^{(\mu)})$ (see also Refs. [28,29]). Here, $\{a,\ b,\ c\}$ denote the $Pbnm$ orthorhombic axes, and $\mu = G,\ A,\ C$ refer to the type of AFM order. For instance, m_c couples bilinearly to both $n_a^{(G)}$ and to $n_b^{(A)}$ via combinations of R_5^- and M_2^+.

These couplings change the form of the free-energy expansion in Eq. (1). Hereafter, we focus on the case where the leading instabilities for $x > 0$ and $x < 0$ are FM with magnetization along the c axis and G-type AFM with magnetization along the a axis since this is the common ground state of most pristine $ATiO_3$ compounds. Denoting $m \equiv m_c$ and $n \equiv n_a^{(G)}$, the free energy becomes

$$f = \frac{a_F}{2} m^2 + \frac{1}{4} m^4 + \frac{a_G}{2} n^2 + \frac{1}{4} n^4 + \frac{\gamma}{2} m^2 n^2 - Rmn, \tag{3}$$

where $\gamma = \gamma_1$ and R is a parameter related to the strength of the R_5^--mode octahedral rotations and the spin-lattice coupling [43].

We can now discuss what happens to the phase diagrams of Figs. 3(a) and 3(b) for $R \neq 0$ (for concreteness, we consider $R > 0$). The first observation is that $m \neq 0$ and $n \neq 0$ everywhere inside the magnetically ordered phase, resulting in a single PM-to-magnetic transition and in the disappearance of the multicritical points. In the case where the unperturbed phase diagram displayed a TCP and two second-order transition lines ($\gamma < 1$), all that remains is a smooth crossover and no phase transitions [Fig. 3(d)]. On the other hand, in the case $\gamma > 1$, the first-order transition line detaches from the PM-to-magnetic transition line [Fig. 3(c)]. While this kills the BCP, it gives rise to a CEP, located where the first-order line terminates. The phase diagram of Fig. 3(c) in the region inside the magnetically ordered state is reminiscent of the liquid-gas phase diagram of water. While the relevant order parameter in the water case is the difference in densities of the two fluid phases, in our magnetic analog, it is the canting of the magnetization, defined as $\theta \equiv \tan^{-1}(m/n)$ (see Fig. 3).

To gain a deeper insight, we first plot in Figs. 4(a) and 4(b) cuts of the phase diagram of Fig. 3(c) that show how the order parameters m and n change as a function of t and x in different regions. Motivated by these results, we introduce a new set of order parameters $\alpha \equiv (m + n)/2$ and $\beta \equiv m - n$. Note from Figs. 4(a) and 4(b) that only β, but not α, jumps across the first-order line. The free-energy expansion becomes

$$f = \Big(\frac{a_F + a_G}{2} - R\Big)\alpha^2 + \frac{1+\gamma}{2}\alpha^4 + \frac{1}{4}\Big(\frac{a_F + a_G}{2} + R\Big)\beta^2 + \frac{1+\gamma}{32}\beta^4 + \frac{a_F - a_G}{2}\alpha\beta + \frac{3-\gamma}{4}\alpha^2\beta^2. \tag{4}$$

Therefore, the transition temperature for α (β) increases (decreases) due to R. Near the CEP, we can eliminate α and obtain a free-energy expansion only in terms of β, $f = \sum_{\nu=0}^{4} b_\nu \beta^\nu$ (see Appendix C for details). The first-order line, where β jumps, is determined by the condition that the odd-power coefficients b_1 and b_3 become zero. Since both are

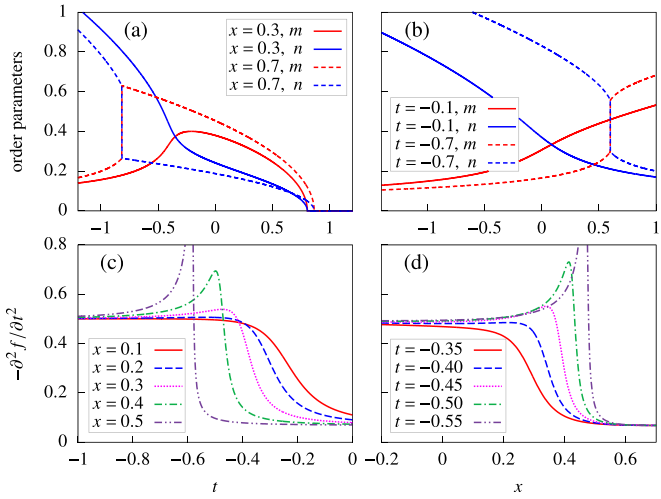

FIG. 4. The ferromagnetic (FM) and antiferromagnetic (AFM) order parameters m and n in the phase diagram of Fig. 3(c), plotted (a) as a function of t for fixed $x$and (b) as a function of x for fixed t. Specific heat $C/T \propto -\partial^2 f/\partial t^2$ (c) as a function of t for fixed x and (d) as a function of x for fixed t. The maxima correspond to the Widom line [dotted line in Fig. 3(c)].

proportional to $a_F - a_G$, this condition gives $a_F = a_G$, leading to

$$x = \frac{2(a-1)}{a+1}t. \tag{5}$$

The position of the CEP is given by combining the above expression with the condition $b_2 = 0$, which yields

$$x_c = -\frac{2(a-1)R}{a(\gamma-1)}, \quad t_c = -\frac{(a+1)R}{a(\gamma-1)}. \tag{6}$$

Along the first-order line, the order parameter β vanishes according to the usual mean-field result $\beta|_{b_1=b_3=0} = \sqrt{-b_2/(2b_4)} \propto (t_c - t)^{1/2}$. Beyond a mean-field approximation, however, the CEP is expected to belong to the Ising universality class. Indeed, by applying the transformation $x = \frac{2}{a+1}x' + (a-1)t'$ and $t = \frac{a+1}{2}t'$, the first-order line becomes the vertical line $x' = 0$ terminating at the CEP at $t'_c = -2R/a(\gamma-1)$. Thus, x' plays a similar role to the magnetic field in the Ising model, and t' to the reduced temperature. In models described by the Ising universality class, a Widom line is expected to emerge from the CEP and to extend to higher temperatures [30–32]. To investigate it, we compute the specific heat $C/T \propto -\partial^2 f/\partial t^2$ as a function of t (or x) for fixed x (or t). As shown in Figs. 4(c) and 4(d), C/T displays a pronounced maximum above the CEP, indicative of the enhanced fluctuations that characterize the Widom line [44]. As one moves farther from the CEP, this C/T maximum becomes weaker, and the Widom line fades away, as shown by the dotted line in the phase diagram of Fig. 3(c).

Our results in Eq. (6) show that the temperature of the CEP decreases linearly with the parameter R. Importantly, the R_5^- rotation mode is very sensitive to the lattice parameters, which opens the possibility of tuning the position of the CEP experimentally by applying uniaxial stress. In Fig. 2(b), we show how the R_5^- mode amplitude changes as a function of uniaxial strain along each one of the three main orthorhombic axes, determined via first-principles calculations for the specific case of $YTiO_3$ (see Appendix B for details). While it is difficult to establish the relative change in R corresponding to the relative change in the mode amplitude without input from microscopics, previous first-principles calculations show that even modest changes of the order of a few percent in the amplitudes of the R_5^- and M_2^+ modes can cause changes of a factor of 2 or more in the exchange parameters [39]. This indicates a strong spin-lattice coupling in rare-earth titanates and the potential to drastically change the temperature of the CEP via uniaxial strain to promote a QCEP. This is also consistent with the strong dependence of the FM transition temperature on uniaxial pressure observed experimentally in $YTiO_3$ [19].

We now discuss some experimental consequences of our results. The existence of a first-order line inside the magnetically ordered state in the chemically substituted rare-earth titanates, such as $Sm_{1-x}Gd_xTiO_3$ and $Y_{1-x}La_xTiO_3$, could be detected by measurements of the temperature dependence of the canting angle, which would jump across the transition line and display hysteresis [45]. Thermodynamic measurements, such as specific heat and magnetic susceptibility, should also display typical signatures of a first-order transition. In the crossover region above the first-order line, the specific heat is expected to display a pronounced maximum near the CEP as the Widom line is crossed, indicative of enhanced fluctuations. While a fine control of the concentration of the substituted rare-earth may be challenging, one can alternatively use uniaxial strain as a tuning parameter to smoothly move a given composition across the first-order and/or Widom lines.

More broadly, for appropriate concentrations, uniaxial strain could even be used to tune the CEP to zero temperature, thus promoting a QCEP. The general properties of a QCEP have been discussed in the context of other materials, most notably quasi-2D organic salts [46] and metallic FMs [33]. In the former, a pressure-induced first-order line separates the PM Mott insulating and metallic phases, and the transition temperature associated with the CEP is very low [47–49]. Behaviors typically associated with quantum criticality have been observed in transport properties in the vicinity of the CEP [46]. In metallic FMs, an external magnetic field can be used to suppress the ferrometamagnetic transition down to $T = 0$ [33]. In the particular case of the bilayer ruthenate $Sr_3Ru_2O_7$, the putative magnetic-field-driven QCEP is preempted by nematic order [50] and is associated with unusual transport and thermodynamic properties [2,51]. Recently, a CEP associated with a first-order QPT was also observed in a frustrated quantum magnet [8]. The rare-earth titanates thus provide a framework to investigate magnetic QCEPs. In contrast to the more usual case of metallic FMs, the metamagnetic transition involves two symmetry-equivalent insulating canted spin states, where orthogonal FM and AFM order parameters coexist. As a result, the dynamical critical exponent of the QCEP is expected to be $z = 1$, placing the system at the upper critical dimension since $d + z = 4$. Another important difference is that the metamagnetic transition can be tuned by strain even in the absence of magnetic fields. Finally, rare-earth titanates can also be doped with charge carriers, which promotes a Mott insulating-to-metal transition [15]. An interesting direction for future studies is to investigate

the fate of the QCEP uncovered here as the system is tuned across the band-filling-driven Mott transition since a metallic QCEP would have fundamentally different dynamics than an insulating one.

ACKNOWLEDGMENTS

We thank A. Chubukov, M. Greven, S. Hameed, A. Najev, and D. Pelc for fruitful discussions. This paper was funded by the U.S. Department of Energy through the University of Minnesota Center for Quantum Materials, under Grant No. DE-SC-0016371.

APPENDIX A: GROUP-THEORY ANALYSIS

The perovskite rare-earth titanates have space group #62 due to the combination of two symmetry-inequivalent rotation patterns of the TiO_6 octahedra. As illustrated in Fig. 2(a), these rotations transform as the M_2^+ and R_5^- irreps of the artificial cubic lattice. The pattern corresponding to the M_2^+ irrep has TiO_6 octahedra which rotate about a single cubic axis, while the rotation pattern corresponding to the R_5^- irrep is composed of a combination of octahedral rotations about both of the remaining cubic axes. Using Glazer notation, we denote these two patterns as $a^0a^0c^+$ and $a^-a^-c^0$, respectively. Since these rotations lower the cubic symmetry, we are free to choose any of the three cubic axes as the axis corresponding to the M_2^+ irrep. In the resulting distorted structure, this axis points along the longest of the orthorhombic lattice vectors. If we choose this axis to be $\boldsymbol{c}$, as we have here, then the resulting $a^-a^-c^+$ tilting pattern takes the $Pm\bar{3}m$ cubic symmetry to the *Pbnm* setting of space group #62. Had we chosen the long axis to point along $\boldsymbol{b}$ (Glazer tilting pattern $a^-c^+a^-$), we would have the standard *Pnma* setting of the same space group. The basis transformation from the standard setting *Pnma* to the nonstandard *Pbnm* is defined by [28]

$$\{\boldsymbol{a}_n, \boldsymbol{b}_n, \boldsymbol{c}_n\} = \{\boldsymbol{a}_s, \boldsymbol{b}_s, \boldsymbol{c}_s\}P, \tag{A1}$$

where

$$P = \begin{pmatrix} 0 & 1 & 0 \\ 0 & 0 & 1 \\ 1 & 0 & 0 \end{pmatrix}, \tag{A2}$$

and the subscripts s and n denote the lattice vectors in the standard and nonstandard settings, respectively.

Using standard group-theory techniques and the ISOTROPY Software Suite [52,53], we determine how the two types of octahedral rotations M_2^+ and R_5^- couple the FM order parameter to the three types of AFM order parameters (G, C, and A type), see also Ref. [28]. As explained in the main text, the FM order parameter transforms as $m\Gamma_4^+$ with respect to symmetry operations of the cubic $Pm\bar{3}m$ space group. Similarly, the G-type AFM order parameter transforms as mR_5^-. These irreps are 3D since the magnetic moments can point along any of the three axes, and the stars of Γ and R contain only one wave vector. The order parameters described by these irreps are shown in Figs. 5(a) and 5(b).

The A-type AFM order parameters have the wave vector $X = (\pi/a, 0, 0)$, which has three vectors in its star. For each of these wave vectors, the magnetic moments can point along three orthogonal directions, and as a result, there are nine possible A-type AFM orders. These orders correspond to the 3D irrep ${}^*mX_1^-$, in which the magnetic moments align along the wave vector direction, and the six-dimensional (6D) irrep ${}^*mX_5^-$, in which the magnetic moments align perpendicular to the wave vector. We use the * symbol to differentiate the representations of the space group, which contain all vectors in the star of a wave vector, from the representations of the little group. For a single wave vector in the star, the magnetic little-group representations mX_1^- and mX_5^- are 1D and 2D, respectively. These modes are depicted in Figs. 5(c) and 5(d). Similarly, the C-type AFM orders, which have one of the three wave vectors in the star of $M = (\pi/a, \pi/a, 0)$, are described by the magnetic space group irreps ${}^*mM_2^+$ (3D) and ${}^*mM_5^+$ (6D), which have magnetic little-group irreps mM_2^+ and mM_5^+ that are 1D and 2D, respectively [Figs. 5(e) and 5(f)].

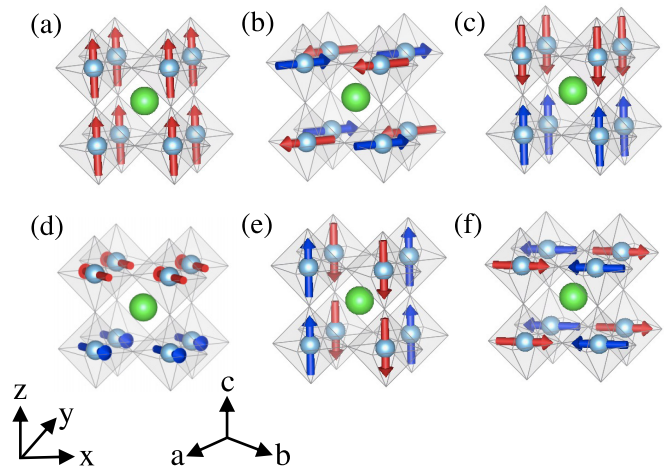

FIG. 5. The magnetic orders considered in this paper, corresponding to the (a) $m\Gamma_4^+$ (FM order), (b) mR_5^- (G-type AFM order), (c) mX_1^- (A-type AFM order), (d) mX_5^- (A-type AFM order), (e) mM_2^+ (C-type AFM order), and (f) mM_5^+ (C-type AFM order) irreps of the cubic $Pm\bar{3}m$ space group. The blue spheres correspond to Ti atoms and the green to the rare-earth atoms.

We consider only the order parameter directions of the above irreps that preserve the translational symmetry of the *Pbnm* structure. For the FM and G-type AFM orders, all three possible moment directions along the orthorhombic axes preserve the symmetry. Therefore, we denote their respective order parameters as (F_a, F_b, F_c) and (G_a, G_b, G_c). These correspond to the $m\Gamma_4^+$ and mR_5^- irreps, respectively, and the subscript denotes along which orthorhombic axis the magnetic moments point.

For A- and C-type AFM orders, because only one vector from the star preserves the translational symmetry of *Pbnm*, it is sufficient to work with the magnetic little groups. In the case of A-type AFM order, the *Pbnm*-preserving configurations consist of moments that alternate along the orthorhombic c axis. Therefore, we denote the order parameters A_c and (A_a, A_b), associated with the mX_1^- and mX_5^- irreps, respectively. Similarly, the translational symmetry-preserving C-type AFM order parameters have a wave vector on the a-b plane and are denoted by C_c and (C_a, C_b), coming from the mM_2^+ and mM_5^+ little-group irreps, respectively. We

TABLE I. Symmetry-allowed third- and fourth-order terms in the free-energy expansion that couple the magnetic order parameters with the octahedral rotation modes in the rare-earth titanates. Note that different subtables correspond to the different magnetic ground states listed in Table II.

Third order	Fourth order
$R_5^- G_a F_c$ $M_2^+ G_a A_b$	$R_5^- M_2^+ A_b F_c$
Third order	Fourth order
$R_5^- F_a G_c$ $M_2^+ F_a C_b$	$R_5^- M_2^+ C_b G_c$
Third order	Fourth order
$R_5^- C_a A_c$ $M_2^+ C_a F_b$	$R_5^- M_2^+ F_b A_c$
Third order	Fourth order
$R_5^- A_a C_c$ $M_2^+ A_a G_b$	$R_5^- M_2^+ C_c G_b$

emphasize that, although we have grouped terms that correspond to the same irrep in the high-symmetry cubic $Pm\bar{3}m$ space group, all order parameters listed here are 1D with respect to the lower-symmetry *Pbnm* space group. That is, no operation in the *Pbnm* space group transforms F_a to F_b, C_a to C_b, etc.

The symmetry-allowed bilinear couplings between the FM and AFM order parameters, mediated by the octahedral rotations, are shown in Table I. They result in four different magnetic ground states that do not break the translational symmetry of the *Pbnm* space group and transform as four different Γ-point irreps of *Pbnm* [28]. Table II lists these four ground states in both *Pbnm* and *Pnma* notations. While our analysis in the main text focused on the $G_aA_bF_c$ ground state, with a G_a-dominated phase crossing over to a F_c-dominated phase, the same conclusions would hold for other combinations of FM and AFM order parameters if they are associated with the same magnetic ground state.

APPENDIX B: FIRST-PRINCIPLES CALCULATIONS

To illustrate how one might experimentally tune the amplitude of the octahedral rotations, we use first-principles calculations to obtain the rotation amplitude R as a function of uniaxial strain applied along the three orthorhombic axes [Fig. 2(b)]. To do this, we fix the strained lattice parameter along an orthorhombic axis to different values while allowing the other two lattice parameters and the internal coordinates of the atoms to relax to minimize the forces on the atoms and the stresses on the unit cell. Density functional theory calculations were performed using the projector augmented wave approach as implemented in the Vienna *Ab Initio* Simulation Package (VASP) [54–56]. These calculations on $YTiO_3$ used the PBEsol exchange-correlation functional [57], a plane-wave cutoff of 550 eV, and a $4 \times 4 \times 4$ Monkhorst-Pack grid. In addition, to properly reproduce the local magnetic moments on the Ti ions, we used the rotationally invariant LSDA + U scheme introduced by Dudarev *et al.* [58] with $U = 4$ eV.

TABLE II. The four different types of translational-symmetry preserving magnetic ground states in the different basis settings of the space group #62.

Pnma	*Pbnm*
$A_aF_bG_c$	$G_aA_bF_c$
$C_aG_bF_c$	$F_aC_bG_c$
$F_aA_bC_c$	$C_aF_bA_c$
$G_aC_bA_c$	$A_aG_bC_c$

In Fig. 2(b), we plot the total displacement amplitude of the R_5^- octahedral rotation mode. While this quantity is proportional to the octahedral rotation angles to first order, it is more well defined. The definition of the octahedral rotation angles can become nonunique when there are multiple different structural distortions that lead to unequal bond lengths, etc., as is the case in $YTiO_3$. The mode amplitude is calculated by projecting the displacements of all atoms to the symmetry-adapted basis modes of the R_5^- irrep and calculating the total magnitude of the projected displacements. We use the ISODISTORT tool [59] for this calculation [60].

APPENDIX C: GINZBURG-LANDAU EXPANSION NEAR THE CEP

The results of Figs. 3 and 4 were obtained through exact numerical minimization. As explained in the main text, to gain deeper insight into the problem, we find it useful to have an analytical description of the CEP that appears when $R \neq 0$. Expanding the free-energy in powers of the rotated order parameters $\alpha = (m+n)/2$ and $\beta = m - n$, which correspond to the high-temperature magnetic transition and the low-temperature first-order transition, respectively, we find

$$f = \left(\frac{a_F + a_G}{2} - R\right)\alpha^2 + \frac{1+\gamma}{2}\alpha^4 + \frac{1}{4}\left(\frac{a_F + a_G}{2} + R\right)\beta^2 + \frac{1+\gamma}{32}\beta^4 + \frac{a_F - a_G}{2}\alpha\beta + \frac{3-\gamma}{4}\alpha^2\beta^2. \tag{C1}$$

Near the CEP ($\beta \ll 1$), we can expand α in powers of β:

$$\alpha = \sum_{\nu=0}^{4} \alpha_\nu \beta^\nu + \mathcal{O}(\beta^5), \tag{C2}$$

where the coefficients α_ν are determined by $\partial_\alpha f = 0$:

$$\alpha_0 = \sqrt{-\frac{a_F + a_G - 2R}{2(1+\gamma)}}, \tag{C3a}$$

$$\alpha_1 = \frac{a_F - a_G}{4(a_F + a_G - 2R)}, \tag{C3b}$$

$$\alpha_2 = \frac{6(1+\gamma)\alpha_1^2 + \frac{3-\gamma}{2}}{2(a_F + a_G - 2R)}\alpha_0, \tag{C3c}$$

$$\alpha_3 = \frac{2(1+\gamma)\left(\alpha_1^2 + 6\alpha_0\alpha_2\right) + \frac{3-\gamma}{2}}{2(a_F + a_G - 2R)}\alpha_1, \tag{C3d}$$

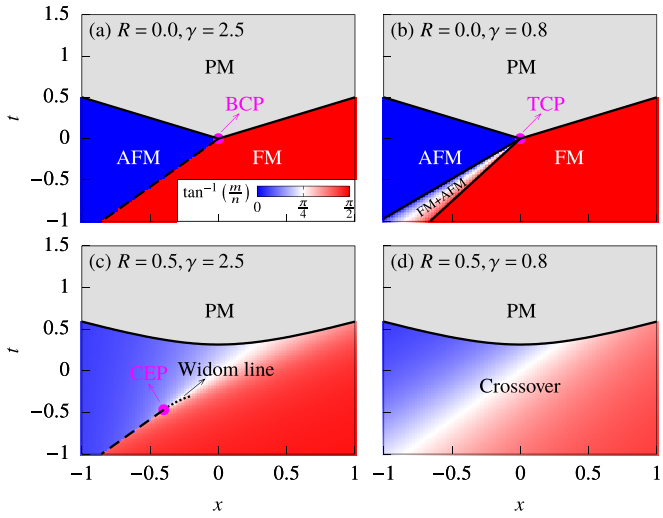

FIG. 6. Phase diagrams obtained by minimizing the free-energy Eq. (3) with $a = 2.5$. The notations follow Fig. 3.

$$\alpha_4 = \frac{6(1+\gamma)\left(\alpha_1^2\alpha_2 + \alpha_0\alpha_2^2 + 2\alpha_0\alpha_1\alpha_3\right) + \frac{3-\gamma}{2}\alpha_2}{2(a_F + a_G - 2R)}. \quad \text{(C3e)}$$

With Eq. (C3), we can eliminate α in the free-energy, leading to a theory with a single variable β:

$$f = \sum_{\nu=0}^{4} b_\nu \beta^\nu + \mathcal{O}(\beta^5), \quad \text{(C4)}$$

with

$$b_0 = -\frac{(a_F + a_G - 2R)^2}{8(1+\gamma)}, \quad \text{(C5a)}$$

$$b_1 = \frac{a_F - a_G}{2}\alpha_0, \quad \text{(C5b)}$$

$$b_2 = \frac{a_F - a_G}{4}\alpha_1 + \frac{(\gamma-1)(a_F + a_G) + 4R}{4(1+\gamma)}, \quad \text{(C5c)}$$

$$b_3 = \left[2(1+\gamma)\alpha_1^2 + \frac{3-\gamma}{2}\right]\alpha_0\alpha_1, \quad \text{(C5d)}$$

$$b_4 = -4(1+\gamma)\alpha_1^4 - \frac{3-\gamma}{2}\alpha_1^2 + \frac{\gamma-1}{4(1+\gamma)}. \quad \text{(C5e)}$$

The first-order line is obtained by imposing $b_1 = b_3 = 0$, which implies $a_F = a_G$. This leads to the $x(t)$ line defined by

$$x = \frac{2(a-1)}{a+1}t, \quad \text{(C6)}$$

where, as in the main text, we used the parametrization:

$$a_F = a\left(t - \frac{x}{2}\right), \qquad a_G = t + \frac{x}{2}. \quad \text{(C7)}$$

The CEP is then obtained by combinining $x = \frac{2(a-1)}{a+1}t$ with $b_2 = 0$, which leads to

$$x_c = -\frac{2(a-1)R}{a(\gamma-1)}, \quad \text{(C8a)}$$

$$t_c = -\frac{(a+1)R}{a(\gamma-1)}. \quad \text{(C8b)}$$

The order parameter along the first-order line is given by $\partial_\beta f = 0$:

$$\beta|_{b_1=b_3=0} = \sqrt{-\frac{b_2}{2b_4}}. \quad \text{(C9)}$$

The parameter $a \equiv a_{F,0}/a_{G,0}$ controls the relative size of the AFM and FM dominated regions but does not affect any other conclusions of this paper. In observation of the experimental phase diagrams where the AFM phase typically occupies a larger area than the FM phase, we used $a = 0.4$ in Fig. 3. Figure 6 shows the effect of choosing a larger value of a, which indeed leads to a larger area occupied by the FM phase.

[1] S. Sachdev, *Quantum Phase Transitions*, 2nd ed. (Cambridge University Press, Cambridge, 2011).

[2] S. A. Grigera, R. S. Perry, A. J. Schofield, M. Chiao, S. R. Julian, G. G. Lonzarich, S. I. Ikeda, Y. Maeno, A. J. Millis, and A. P. Mackenzie, Science **294**, 329 (2001).

[3] A. Abanov, A. V. Chubukov, and J. Schmalian, Adv. Phys. **52**, 119 (2003).

[4] T. Senthil, A. Vishwanath, L. Balents, S. Sachdev, and M. P. A. Fisher, Science **303**, 1490 (2004).

[5] H. v. Löhneysen, A. Rosch, M. Vojta, and P. Wölfle, Rev. Mod. Phys. **79**, 1015 (2007).

[6] C. Rüegg, B. Normand, M. Matsumoto, A. Furrer, D. F. McMorrow, K. W. Krämer, H. U. Güdel, S. N. Gvasaliya, H. Mutka, and M. Boehm, Phys. Rev. Lett. **100**, 205701 (2008).

[7] R. Coldea, D. A. Tennant, E. M. Wheeler, E. Wawrzynska, D. Prabhakaran, M. Telling, K. Habicht, P. Smeibidl, and K. Kiefer, Science **327**, 177 (2010).

[8] J. L. Jiménez, S. P. G. Crone, E. Fogh, M. E. Zayed, R. Lortz, E. Pomjakushina, K. Conder, A. M. Läuchli, L. Weber, S. Wessel, A. Honecker, B. Normand, C. Rüegg, P. Corboz, H. M. Rønnow, and F. Mila, Nature (London) **592**, 370 (2021).

[9] M. Imada, A. Fujimori, and Y. Tokura, Rev. Mod. Phys. **70**, 1039 (1998).

[10] P. A. Lee, N. Nagaosa, and X.-G. Wen, Rev. Mod. Phys. **78**, 17 (2006).

[11] M. Mochizuki and M. Imada, New J. Phys. **6**, 154 (2004).

[12] J. Goral, J. Greedan, and D. MacLean, J. Solid State Chem. **43**, 244 (1982).

[13] J. Greedan, J. Less-Common Met. **111**, 335 (1985).

[14] Y. Okimoto, T. Katsufuji, Y. Okada, T. Arima, and Y. Tokura, Phys. Rev. B **51**, 9581 (1995).

[15] T. Katsufuji, Y. Taguchi, and Y. Tokura, Phys. Rev. B **56**, 10145 (1997).

[16] G. Amow, J.-S. Zhou, and J. Goodenough, J. Solid State Chem. **154**, 619 (2000).

[17] H. D. Zhou and J. B. Goodenough, Phys. Rev. B **71**, 184431 (2005).

[18] S. Hameed, S. El-Khatib, K. P. Olson, B. Yu, T. J. Williams, T. Hong, Q. Sheng, K. Yamakawa, J. Zang, Y. J. Uemura, G. Q. Zhao, C. Q. Jin, L. Fu, Y. Gu, F. Ning, Y. Cai, K. M. Kojima, J. W. Freeland, M. Matsuda, C. Leighton *et al.*, Phys. Rev. B **104**, 024410 (2021).

[19] W. Knafo, C. Meingast, A. V. Boris, P. Popovich, N. N. Kovaleva, P. Yordanov, A. Maljuk, R. K. Kremer, H. v. Löhneysen, and B. Keimer, Phys. Rev. B **79**, 054431 (2009).

[20] T. Mizokawa and A. Fujimori, Phys. Rev. B **54**, 5368 (1996).

[21] M. Itoh, M. Tsuchiya, H. Tanaka, and K. Motoya, J. Phys. Soc. Jpn. **68**, 2783 (1999).

[22] B. Keimer, D. Casa, A. Ivanov, J. W. Lynn, M. v. Zimmermann, J. P. Hill, D. Gibbs, Y. Taguchi, and Y. Tokura, Phys. Rev. Lett. **85**, 3946 (2000).

[23] G. Khaliullin and S. Maekawa, Phys. Rev. Lett. **85**, 3950 (2000).

[24] J. Hemberger, H.-A. Kruj von Nidda, V. Fritsch, J. Deisenhofer, S. Lobina, T. Rudolf, P. Lunkenheimer, F. Lichtenberg, A. Loidl, D. Bruns, and B. Büchner, Phys. Rev. Lett. **91**, 066403 (2003).

[25] J. Varignon, M. N. Grisolia, D. Preziosi, P. Ghosez, and M. Bibes, Phys. Rev. B **96**, 235106 (2017).

[26] Z. Y. Zhao, O. Khosravani, M. Lee, L. Balicas, X. F. Sun, J. G. Cheng, J. Brooks, H. D. Zhou, and E. S. Choi, Phys. Rev. B **91**, 161106(R) (2015).

[27] B. Li, D. Louca, J. Niedziela, Z. Li, L. Zhang, J. Zhou, and J. B. Goodenough, Phys. Rev. B **94**, 224301 (2016).

[28] R. Schmitz, O. Entin-Wohlman, A. Aharony, A. B. Harris, and E. Müller-Hartmann, Phys. Rev. B **71**, 144412 (2005).

[29] E. Bousquet and N. Spaldin, Phys. Rev. Lett. **107**, 197603 (2011).

[30] G. O. Jones and P. A. Walker, Proc. Phys. Soc. B **69**, 1348 (1956).

[31] L. Xu, P. Kumar, S. V. Buldyrev, S.-H. Chen, P. H. Poole, F. Sciortino, and H. E. Stanley, Proc. Natl. Acad. Sci. USA **102**, 16558 (2005).

[32] G. G. Simeoni, T. Bryk, F. A. Gorelli, M. Krisch, G. Ruocco, M. Santoro, and T. Scopigno, Nat. Phys. **6**, 503 (2010).

[33] M. Brando, D. Belitz, F. M. Grosche, and T. R. Kirkpatrick, Rev. Mod. Phys. **88**, 025006 (2016).

[34] J.-H. Chu, H.-H. Kuo, J. G. Analytis, and I. R. Fisher, Science **337**, 710 (2012).

[35] A. Steppke, L. Zhao, M. E. Barber, T. Scaffidi, F. Jerzembeck, H. Rosner, A. S. Gibbs, Y. Maeno, S. H. Simon, A. P. Mackenzie, and C. W. Hicks, Science **355**, eaaf9398 (2017).

[36] Y. Sato, S. Kasahara, H. Murayama, Y. Kasahara, E.-G. Moon, T. Nishizaki, T. Loew, J. Porras, B. Keimer, T. Shibauchi, and Y. Matsuda, Nat. Phys. **13**, 1074 (2017).

[37] D. Pelc, Z. Anderson, B. Yu, C. Leighton, and M. Greven, Nat. Commun. **10**, 2729 (2019).

[38] S. Hameed, D. Pelc, Z. W. Anderson, A. Klein, R. J. Spieker, L. Yue, B. Das J. Ramberger, M. Lukas, Y. Liu, M. J. Krogstad, R. Osborn, Y. Li, C. Leighton, R. M. Fernandes, and M. Greven, Nat. Mater., **21**, 54 (2022).

[39] A. Najev, S. Hameed, D. M. Gautreau, Z. Wang, J. Joe, M. Požek, T. Birol, R. M. Fernandes, M. Greven, and D. Pelc, arXiv:2105.06695.

[40] M. Mochizuki and M. Imada, Phys. Rev. Lett. **91**, 167203 (2003).

[41] K.-S. Liu and M. E. Fisher, J. Low Temp. Phys. **10**, 655 (1973).

[42] A. Aharony, J. Stat. Phys. **110**, 659 (2003).

[43] T. Birol, N. A. Benedek, H. Das, A. L. Wysocki, A. T. Mulder, B. M. Abbett, E. H. Smith, S. Ghosh, and C. J. Fennie, Curr. Opin. Solid State Mater. Sci. **16**, 227 (2012).

[44] The Widom line defined by the maxima in Fig. 4(c) deviates slightly from the one defined by the maxima in Fig. 4(d) since they are not generally local maxima in the 2D $\{x, t\}$ space.

[45] In compounds like $Sm_{1-x}Gd_xTiO_3$, the rare-earth atoms possess magnetic moments and order magnetically [16,61]. Our conclusions remain qualitatively the same if the CEP takes place above the ordering temperature of the rare-earth atoms or when the ordering of the rare-earth atoms is a secondary effect induced by coupling between rare-earth and Ti atoms.

[46] T. Furukawa, K. Miyagawa, H. Taniguchi, R. Kato, and K. Kanoda, Nat. Phys. **11**, 221 (2015).

[47] H. Terletska, J. Vučičević, D. Tanasković, and V. Dobrosavljević, Phys. Rev. Lett. **107**, 026401 (2011).

[48] G. Sordi, K. Haule, and A.-M. S. Tremblay, Phys. Rev. Lett. **104**, 226402 (2010).

[49] H. Eisenlohr, S.-S. B. Lee, and M. Vojta, Phys. Rev. B **100**, 155152 (2019).

[50] R. A. Borzi, S. A. Grigera, J. Farrell, R. S. Perry, S. J. S. Lister, S. L. Lee, D. A. Tennant, Y. Maeno, and A. P. Mackenzie, Science **315**, 214 (2007).

[51] A. J. Millis, A. J. Schofield, G. G. Lonzarich, and S. A. Grigera, Phys. Rev. Lett. **88**, 217204 (2002).

[52] H. T. Stokes, D. M. Hatch, and B. J. Campbell, ISOSUBGROUP, ISOTROPY Software Suite, https://iso.byu.edu.

[53] H. T. Stokes, S. van Orden, and B. J. Campbell, J. Appl. Crystallogr. **49**, 1849 (2016).

[54] G. Kresse and J. Hafner, Phys. Rev. B **47**, 558 (1993).

[55] G. Kresse and J. Furthmüller, Comput. Mater. Sci. **6**, 15 (1996).

[56] G. Kresse and J. Furthmüller, Phys. Rev. B **54**, 11169 (1996).

[57] J. P. Perdew, A. Ruzsinszky, G. I. Csonka, O. A. Vydrov, G. E. Scuseria, L. A. Constantin, X. Zhou, and K. Burke, Phys. Rev. Lett. **100**, 136406 (2008).

[58] S. L. Dudarev, G. A. Botton, S. Y. Savrasov, C. J. Humphreys, and A. P. Sutton, Phys. Rev. B **57**, 1505 (1998).

[59] B. J. Campbell, H. T. Stokes, D. E. Tanner, and D. M. Hatch, J. Appl. Crystallogr. **39**, 607 (2006).

[60] The details of the procedure can be found in https://stokes.byu.edu/iso/isodistorthelp.php.

[61] H. D. Zhou and J. B. Goodenough, J. Phys.: Condens. Matter **17**, 7395 (2005).